MATERIALS SCIENCE

An elastomer with ultrahigh strain-induced crystallization

Chase M. Hartquist[1]†, Shaoting Lin[1]†‡, James H. Zhang[1], Shu Wang[1], Michael Rubinstein[2,3]*, Xuanhe Zhao[1,4]*

Strain-induced crystallization (SIC) prevalently strengthens, toughens, and enables an elastocaloric effect in elastomers. However, the crystallinity induced by mechanical stretching in common elastomers (e.g., natural rubber) is typically below 20%, and the stretchability plateaus due to trapped entanglements. We report a class of elastomers formed by end-linking and then deswelling star polymers with low defects and no trapped entanglements, which achieve strain-induced crystallinity of up to 50%. The deswollen end-linked star elastomer (DELSE) reaches an ultrahigh stretchability of 12.4 to 33.3, scaling beyond the saturated limit of common elastomers. The DELSE also exhibits a high fracture energy of 4.2 to 4.5 kJ m^{-2} while maintaining low hysteresis. The heightened SIC and stretchability synergistically promote a high elastocaloric effect with an adiabatic temperature change of 9.3°C.

INTRODUCTION

Strain-induced crystallization (SIC) is a prevalent phenomenon in elastomers and gels where amorphous polymer chains transform into highly oriented and aligned crystalline domains due to an applied mechanical strain (*1*). Since these oriented and aligned crystalline domains can resist crack extension, promote crack blunting, and facilitate crack deflection (*2*, *3*), SIC remarkably reinforces elastomers and gels, giving increased strength and toughness (*4*). Soft materials are typically reinforced with dissipation mechanisms (*5*–*11*) by inducing viscoelasticity or the Mullins effect, which require substantial recovery time and cause internal damage. In contrast, SIC—as a rapid reinforcement strategy—can preserve network integrity and achieve close to 100% recovery in seconds (*12*, *13*). In addition to its impacts on material reinforcement, SIC plays a vital role in various applications, including elastocaloric cooling (*14*–*16*) and strain-programmable actuation (*17*).

The strain-induced crystallinity in common elastomers is typically below 20%. For instance, natural rubber (NR) only achieves about 15% crystallinity when stretched six times its initial length at room temperature (*18*). Mechanical training (*19*) or freeze-assisted salting out (*20*) of polyvinyl alcohol (PVA) hydrogels can increase the crystallinity to about 40%, but these processes create permanent structural changes. Similarly, the crystallinity of plastics (*21*), fibers (*22*), and polymer solutions (*23*) can irreversibly rise due to mechanical loading. In these cases, the newly formed crystalline domains do not revert to amorphous chains when unloaded. Recent studies report that poly(ethylene glycol) (PEG) hydrogels with slide-ring or tri-branched architectures achieve reversible SIC under large deformations but rely on the presence of a solvent (*12*, *13*). The irreversibility, low magnitude of strain-induced crystallinity, or solvent dependency in soft materials substantially limits their performance for diverse applications. For example, although elastocaloric cooling by SIC in NR was first studied as early as 1805 (*24*), commercialization of elastomer-based elastocaloric refrigeration has been hampered by deficient SIC. It remains technologically challenging yet highly desirable to design soft materials with high, elastically reversible SIC.

Here, we report a class of deswollen end-linked star elastomers (DELSEs) that achieve up to 50% strain-induced crystallinity. We attribute the ultrahigh SIC in the DELSE to two characteristics that differ for conventional elastomers: a uniform network structure and a high stretchability due to the lack of trapped entanglements (*25*, *26*). We take advantage of tetra-PEG gels pioneered by Sakai and colleagues because the network contains a regular structure with fewer defects than common networks and attains elasticity consistent with the phantom network model (Fig. 1A) (*25*–*28*). We show here that a DELSE can, unlike the tetra-PEG gel or common elastomers, achieve ultrahigh SIC. In contrast to the DELSE, common elastomers contain a widely dispersed chain length distribution, substantial molecular defects, and considerable trapped chain entanglements because they are synthesized by either vulcanization or gelation at relatively high concentrations (Fig. 1B). Second, we find that the root mean square (RMS) end-to-end distance of polymer chains in the DELSE when fully deswollen from the overlap concentration is $R(\Phi = 1) \approx \nu_{mon}{}^{1/3} N^{1/3}$, where ν_{mon} is the Kuhn monomer volume and N is the number of Kuhn monomers per chain (Fig. 1E) (see the Supplementary Materials for derivation) (*29*); common elastomers typically have $R(\Phi = 1) \approx N^{1/2}b$, namely, that of unperturbed Gaussian chains (Fig. 1G), where b is the Kuhn length (*30*, *31*). We used molecular dynamics to calculate the average end-to-end distance of polymer chains in the DELSE compared with conventional polymer melts, validating the scaling of $R(\Phi = 1) \sim N^{1/3}$ (Fig. 1, F and H). Because of this scaling and the lack of trapped entanglements, the bulk stretchability is much higher in the DELSE than in common elastomers. The former scales as $N^{2/3}$ without an upper limit, while the latter scales as

[1]Department of Mechanical Engineering, Massachusetts Institute of Technology, Cambridge, MA, USA. [2]Departments of Mechanical Engineering and Materials Science, Biomedical Engineering, Chemistry, and Physics, Duke University, Durham, NC, USA. [3]Institute for Chemical Reaction Design and Discovery, Hokkaido University, Sapporo, Japan. [4]Department of Civil and Environmental Engineering, Massachusetts Institute of Technology, Cambridge, MA, USA.
*Corresponding author. Email: zhaox@mit.edu (X.Z.); michael.rubinstein@duke.edu (M.R.)
†These authors contributed equally to this work.
‡Present address: Department of Mechanical Engineering, Michigan State University, East Lansing, MI, USA.

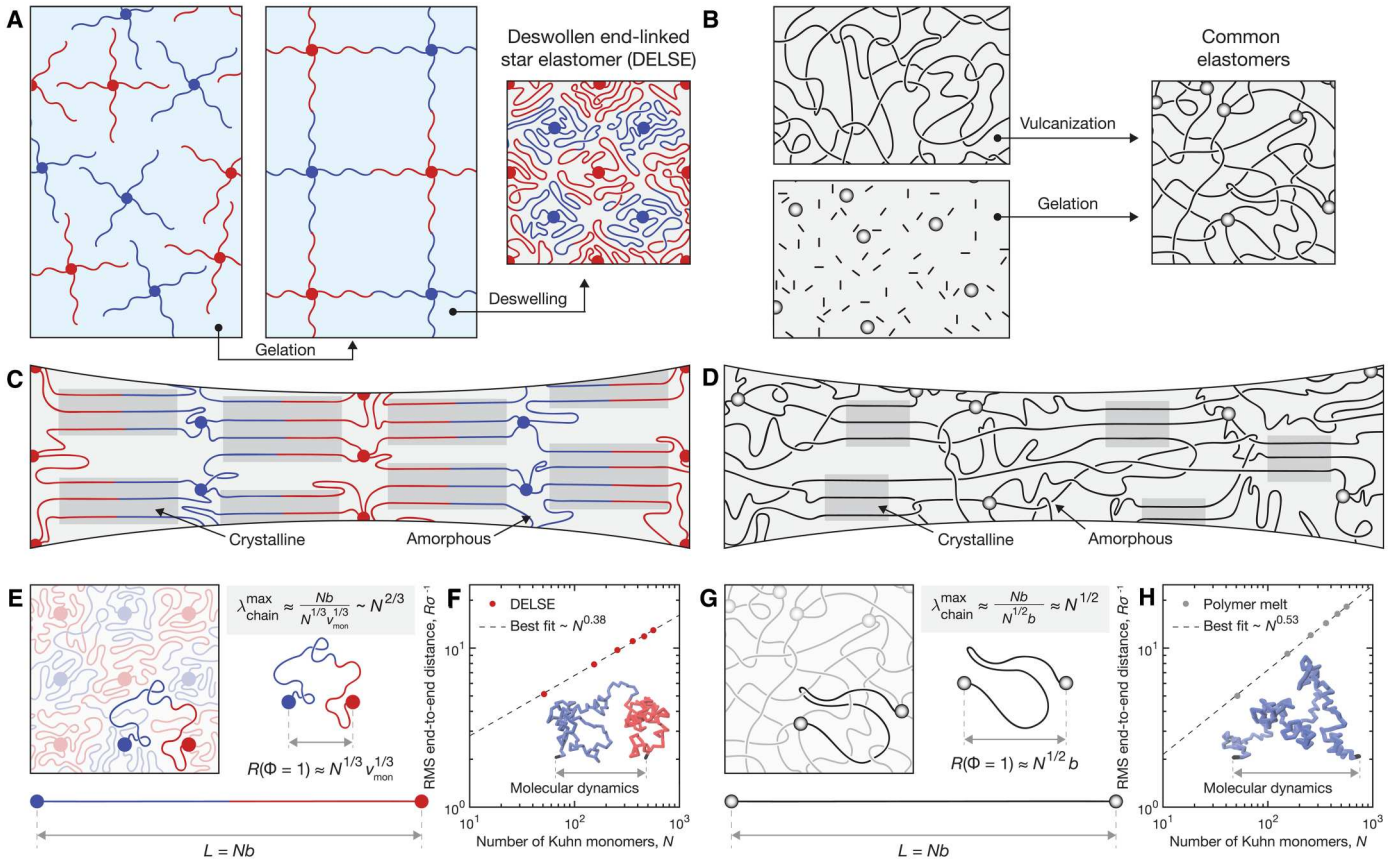

Fig. 1. Deswollen end-linked star elastomers. (**A**) The DELSE forms through controlled crosslinking of star macromers followed by solvent evaporation to form a homogeneous crosslinked polymer network (illustrations are exaggerated to highlight architectural differences). (**B**) Conventional elastomers form through random crosslinking processes such as vulcanization of long polymer chains or gelation from monomers. (**C**) The more homogeneous architecture supports chain alignment during stretching causing crystalline domain formation in the DELSE. (**D**) In contrast, physical barriers like trapped entanglements and inhomogeneities limit the effect of SIC in common elastomers. (**E**) The RMS end-to-end distance of polymers chains in a DELSE in the undeformed state scales as $N^{1/3}$, as validated by (**F**) molecular dynamics simulation (representative simulated chain conformation inset). (**G**) The RMS end-to-end distance of polymers chains in a conventional elastomer in the undeformed state scales as $N^{1/2}$, as validated by (**H**) molecular dynamics simulation (representative simulated chain conformation inset).

$N^{1/2}$ and saturates at $N_e^{1/2}$ when $N > N_e$, where N_e is the entanglement molecular weight. We propose that these features of the DELSE above T_m effectively promote uniform polymer chain orientation and alignment under an applied bulk strain, causing the ultrahigh SIC (Fig. 1, C and D).

RESULTS

Elastomer synthesis

The DELSE was fabricated by evaporating the solvent (i.e., water) from an A-B type tetra-arm PEG hydrogel containing two types of macromers with the same molecular weights: one is terminated by four amine compounds and the other by four N-hydroxysuccinimide (NHS) compounds (Fig. 1A) (*25*, *26*). The A-B type PEG hydrogel synthesis began with mixing the two macromer types into aqueous buffers. The macromer concentrations were each set so crosslinking occurs at the overlap concentration (c^*) to avoid entanglements. The critical overlap concentrations were determined from previously reported viscometry measurements (*25*). The amine terminal group reacts with the NHS ester to form a stable amide bond as the chemical cross-link. The shear modulus of A-B type PEG hydrogels was measured and compared to phantom network theory to validate that the gels achieve a high reaction efficiency following the protocol of Lin *et al.* (*32*). Upon uniform solvent evaporation, the hydrogel isotropically shrank, resulting in a DELSE with a crystalline melting temperature T_m around 45°C (*26*)—as validated by differential scanning calorimetry (DSC) (see fig. S21)—and a loopy globule structure (*33*). Above T_m (60°C), the storage modulus (E') remained constant with frequency variation from 0.01 to 10 Hz as revealed by dynamic mechanical analysis (DMA) (see fig. S16C). The loss modulus (E'') is about two orders of magnitude smaller than the storage modulus, suggesting the elastomer has a low fraction of defects and low hysteresis. A regular PEG deswollen end-linked elastomer (DELE) was fabricated as a control through a similar A-B type reaction of linear NHS-terminated macromers and trifunctional amine-terminated small molecules and deswollen (see the Supplementary Materials for details). The loss modulus for this network is just one order of magnitude smaller than the storage modulus, and direct measurements show large hysteresis, indicating that it contains many defects. Common elastomers like NR exhibit a comparable loss tangent ($\tan \delta = E''/E'$), showing that they have a similar defect density

(see fig. S23). Detailed dynamic rheological analysis can be found in the Supplementary Materials.

Strain-induced crystallization

We first performed small-angle x-ray scattering and wide-angle x-ray scattering (SAXS and WAXS) to measure SIC in the DELSE and compared the results with NR, an elastomer known for SIC, and the regular DELE. DELSE samples with a macromer molecular weight of 20,000 g/mol (10,000 g/mol per individual chain) were uniaxially extended to various stretch levels above T_m normalized by their bulk stretchability λ_1^{max}. Diffraction peaks appear in WAXS intensity plots when stretched past a critical threshold, indicating the formation of crystalline domains (Fig. 2A). The effect of thermal history on structural composition was evaluated to ensure that samples were tested at steady state (see fig. S9). Unstretched DELSE, DELE, and NR rubber samples display broad intensity distributions, indicating their amorphous nature. Although each highly stretched sample shows the formation of narrow peaks caused by crystalline domain formation, the magnitude of the crystalline compared to the amorphous contribution of the DELSE outweighs the effect shown in NR and the DELE (Fig. 2, B, C, and F). These amorphous and crystalline contributions were fitted with Gaussian or pseudo-Voigt functions from WAXS intensity distributions to quantify the SIC (see fig. S2). The crystallinity index is

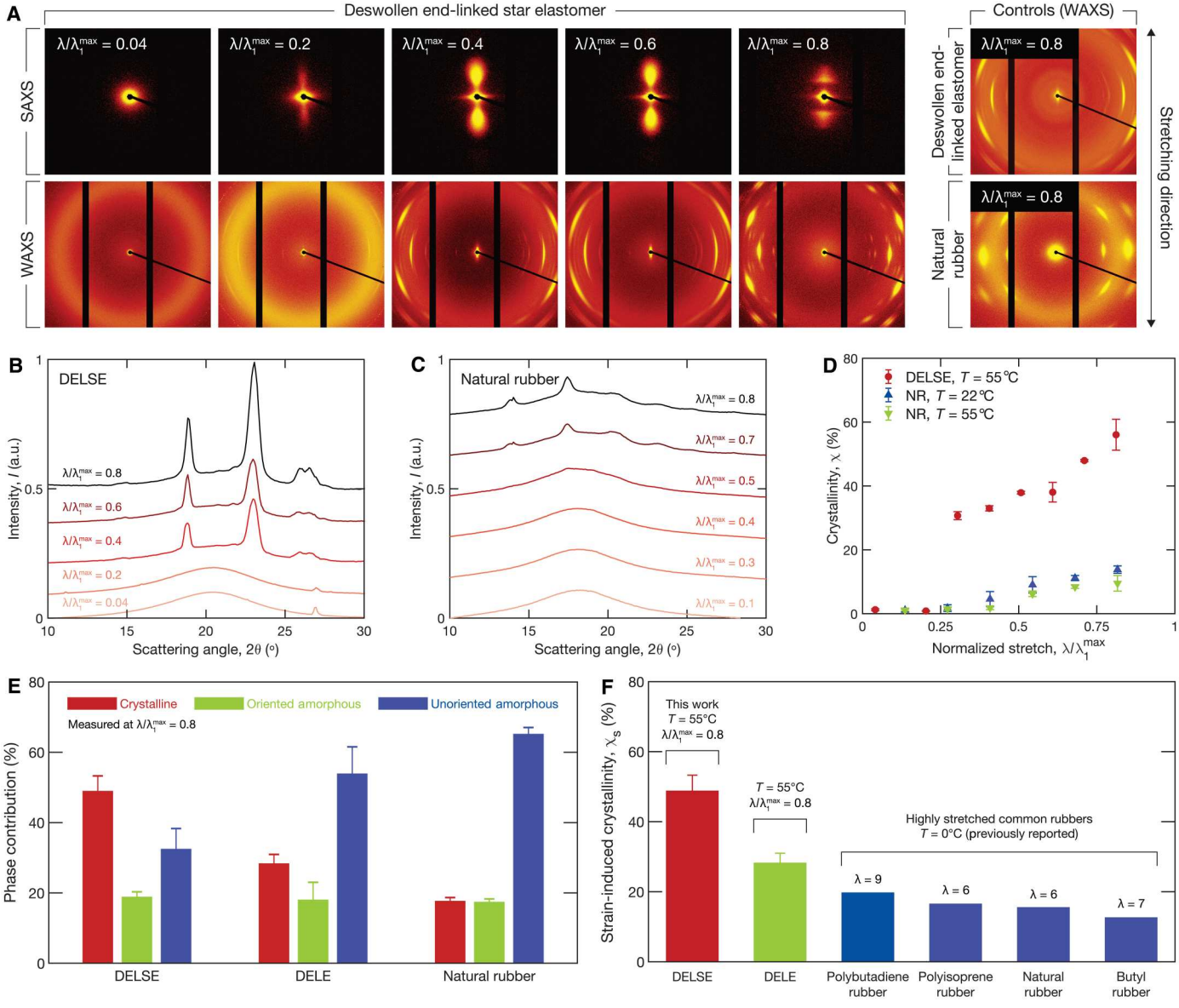

Fig. 2. Ultrahigh SIC of the DELSE. (**A**) WAXS and SAXS patterns show structural development of the DELSE at 55°C compared to the DELE at 55°C and NR at 22°C when mechanically stretched. The WAXS intensity profile develops crystalline peaks for (**B**) the DELSE and (**C**) NR during stretching. (**D**) The crystallinity index increases more dramatically for the DELSE compared to NR. (**E**) Deconvolution of WAXS scans gives the distribution of oriented and unoriented phases. (**F**) Strain-induced crystallinity of the DELSE measured from WAXS pattern deconvolution is compared to the DELE and reported values for various common rubbers with SIC (*18*). Error bars denote standard deviations.

classically defined by a ratio between the integrated areas of the crystalline and amorphous contributions as $\chi = A_C/(A_C + A_A)$. We found that the DELSE achieves up to 50% crystallinity when stretched to ~$0.8\lambda_1^{max}$ above T_m at 55°C (Fig. 2D), markedly outperforming that of the DELE (i.e., 28% at 55°C, ~$0.8\lambda_1^{max}$), NR (i.e., 14% at 22°C, ~$0.8\lambda_1^{max}$ and 10% at 55°C, ~$0.8\lambda_1^{max}$), and other well-studied elastomers including butyl rubber, polyisoprene rubber, and polybutadiene rubber (Fig. 2, E and F).

We further studied the crystal structure formed under stretching through detailed x-ray analysis. The DELSE displays a diffraction spot corresponding to the (120) reflection perpendicular to the stretching direction and a series of spots at the ($\bar{1}$32), (032), ($\bar{2}$12), and (112) reflections (see fig. S6). Additional minor peaks indicating ($\bar{1}$24), ($\bar{2}$04), (004), ($\bar{2}$24), and (024) reflections also appear. Together, these diffraction spots mark the formation of poly(ethylene oxide) crystals with a (7/2) helical structure (*34*–*36*). The DELE displays comparable diffraction peaks due to chemical similarities. We further analyzed the azimuthal spread of diffraction peak intensity to characterize the orientation of crystalline and amorphous domains. The orientational order of crystalline domains was first assessed using the Hermans′ orientation parameter. Crystalline domains formed by uniaxial stretching in the DELSE and NR achieved an orientation order greater than 0.99, reinforcing the concept that SIC forms from alignment of polymer chains in the stretching direction (see fig. S7). Next, a two-dimensional (2D) deconvolution technique that deconstructs WAXS scans quantifies the oriented amorphous regime that forms from aligned chains that have not yet crystallized in highly deformed rubbers (*37*, *38*). We replicated this procedure and verified it with NR (*18*) to study the effect of orientation in the DELSE compared to other rubbers (see fig. S8). From this, we found that the DELSE has considerably less isotropic amorphous polymer content than the DELE and NR (32.4% versus 53.8% and 65.1%, respectively) when highly stretched. In addition to outperforming common rubbers, a direct comparison with the DELE, which has similar chemistry and stretchability, indicates that the more regular network architecture also increases the effect of SIC. These analyses show how the structure and stretchability of the DELSE promote higher strain-induced crystallinity than common elastomers (Fig. 2F).

Mechanical performance

Next, we performed mechanical characterization at 60°C to investigate how ultrahigh SIC in the DELSE effectively promotes high toughness with low stress-stretch hysteresis. Most soft materials are reinforced by introducing sacrificial or reversible bonds, which induce large stress-stretch hysteresis. Different from these classical toughening strategies, the SIC in the DELSE involves little stress-stretch hysteresis (0.05) (Fig. 3A and fig. S14B). The hysteresis of the DELSE at different molecular weights is also low compared to the DELE (fig. S15) and NR (fig. S22). Despite the low stress-stretch hysteresis, the DELSE exhibits a remarkably high fracture energy of up to 4.5 kJ m^{-2} and work to rupture of up to 24.6 MJ m^{-3} (Fig. 3B). The work to rupture notably increases with macromer chain length (fig. S17). The DELSE exhibits a similar storage modulus to the DELE (fig. S16), yet a lower modulus compared with NR, which could possibly be attributed to the reduced chain density and absence of trapped entanglements (fig. S23). When a notched DELSE is subject to tensile loading, the crack initiates in the amorphous material but gets blunted by opaque formation of crystallites, which impedes the crack from propagating (Fig. 3D). We further performed x-ray diffraction on notched DELSE samples at 55°C to measure the strain-induced crystallinity around the crack tip and found that three distinct domains appear: zero SIC at low strains, crack-tip SIC at intermediate strains, and ultrahigh crack-tip and bulk SIC at high strains (Fig. 3C). At high strains, crystalline domains at the crack-tip blunt the crack to a high enough degree that bulk SIC can form to protect the rest of the network.

We further investigated the stretchability of the DELSE. For common elastomers, since the end-to-end distances of polymer chains in the undeformed and straightened states are $N^{1/2}b$ and Nb, the stretchability of polymer chains scales with $N^{1/2}$ and saturates at $N_e^{1/2}$ when $N > N_e$ due to the trapped entanglements formed during preparation (*11*, *30*, *31*, *39*). For the DELSE, due to the deswelling, the RMS end-to-end distance of polymer chains in the undeformed state scales with $N^{1/3}$, so the stretchability of polymer chains increases to scale with $N^{2/3}$ beyond the entanglement threshold in common elastomers. We measured the stretchability of the DELSE with different macromer molecular weights. Our experimentally measured stretchability scales with $N^{0.72}$, clearly exceeding $N^{1/2}$ (Fig. 4). The discrepancy possibly occurs due to imperfect reaction efficiency or physical internal constraints restricting every chain from fully aligning. Sakai and colleagues observed a similar scaling in tetra-arm PEG hydrogels (*29*) with varying polymer volume fraction (*40*). These findings suggest that DELSEs stretch beyond the limits of entangled networks, a feature deemed useful for applications like solid-state cooling.

Elastocaloric cooling

To validate its potential for use as a caloric material for solid-state cooling applications, we further studied the elastocaloric effect in the DELSE compared with NR. An ideal elastocaloric cooling cycle harnesses the decrease in conformation entropy to increase thermal entropy and heat the bulk material. In elastomers with SIC, an additional latent heat contribution of crystallite formation heightens this effect. The increased stretchability, ultrahigh SIC, and uniform chain length distribution of the DELSE synergistically increase the theoretical elastocaloric effect compared to conventional elastomers (Fig. 5A). We measured the adiabatic temperature change of the DELSE and NR with an infrared camera during rapid unloading in a custom stretching device (Fig. 5B). The DELSE achieved a 9.3°C temperature change when unloaded from 54.5°C (Fig. 5C). NR cooled by 3.5°C from 53.5°C (Fig. 5D), which is within 2°C of published results at 49°C at a higher strain rate of 20 s^{-1} (*41*). We assert that DELSEs make strong candidates for advanced solid-state cooling technology since they can attain higher configurational entropy and crystallinity changes during mechanical loading than conventional elastomers.

DISCUSSION

Comparisons between the DELSE and NR show how increased stretchability, different polymer chemistry, and a more well-formed structure combinatorially increase the SIC and elastocaloric effect in elastomeric materials. The additional comparison with the DELE, whose stretchability and chemistry parallel those of the DELSE, specifically demonstrates the importance of the relatively

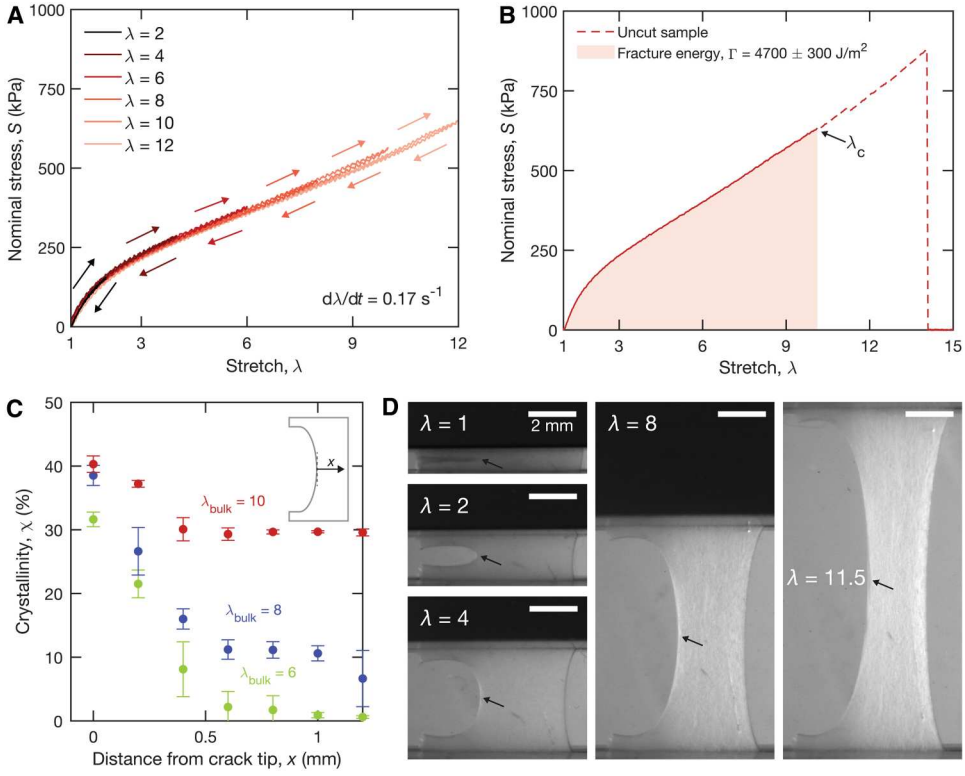

Fig. 3. Mechanical behavior of the DELSE. (**A**) Cyclic loading and unloading of the DELSE with 10,000 g mol^{-1} molecular weight indicates negligible hysteresis at 60°C. (**B**) The measured fracture energy Γ is 4.7 kJ m^{-2}. (**C**) Heightened SIC occurs near the crack tip when measured at 55°C, giving (**D**) crack blunting and increased opacity in the material (arrows mark the crack tip). Error bars denote standard deviations.

homogeneous structure. The DELE also exhibits higher SIC than NR due to its stretchability and chemistry; however, the DELSE outperforms the DELE because it is more homogeneous and contains fewer defects.

Since Katz first noticed a rubber band become opaque due to SIC during stretching in 1924 (*1*), rubbers have been harnessed throughout society for everything from household goods to car tires, etc. Although applications for rubber have progressed in the modern era, the synthesis strategy has remained almost the same. Here, we report the next generation of elastomers that demonstrate profound SIC, far exceeding that of NR and other common elastomers. The DELSEs also warrant further fundamental investigation due to the abnormal scaling of their elastic stretchability limit. Generally, the elastomer fabrication approach harnessed here—end-linking a highly regular gel and then fully deswelling the network—provides a platform with promise across a breadth of polymer chemistries. As shown here in the DELSE, elastomers fabricated in this manner exhibit the capacity to outperform conventional counterparts. These results also suggest the potential for precisely engineering SIC in soft materials by controlling their network architecture. This class of deswollen elastomers can play a key role in the future of aerospace structures, medical devices, and elastocaloric refrigeration design.

MATERIALS AND METHODS

DELSE fabrication

The DELSE was prepared by dehydrating an end-linked star hydrogel (fig. S1A) (*25*, *26*). The hydrogel was formed from an A-B type reaction of commercially available tetra-amine–terminated and tetra-NHS–terminated polyethylene glycol (PEG) macromers (4arm-PEG-NH_2 and 4arm-PEG-NHS, Laysan Bio and JenKem Technology) with 5000, 10,000, 20,000, and 40,000 g/mol macromer molecular weights or 2500, 5000, 10,000, and 20,000 g/mol per chain, respectively. Hydrogel synthesis follows reported protocols (*32*, *42*). Tetra-amine–terminated PEG (100 mg) was dissolved in a 1-ml phosphate aqueous buffer (good solvent) with a pH of 7.4 and ionic strength of 100 mM and thoroughly mixed (*43*). The pH was tuned with trace amounts of sodium hydroxide (NaOH) between 7.4 and 8.0 to produce the highest reaction efficiency (e.g., $p \sim 0.9$ for M_W = 10,000 g/mol). This solution was stored for 30 min and briefly sonicated (~5 s). Next, 100 mg of tetra-NHS–terminated PEG was dissolved in a 1-ml phosphate–citric acid aqueous buffer with a pH of 5.8 and ionic strength of 100 mM, thoroughly mixed, and quickly sonicated (~5 s). Both solutions were carefully degassed and then quickly mixed within 5 min of dissolving the tetra-NHS–terminated PEG to achieve crosslinking around the overlap concentration (c^*). The overlap concentration was measured in the literature by viscometry; the intercept was determined by measuring and fitting viscosities of the A- and B-type macromers as a function of concentration (*25*). The samples were poured over a 40 mm × 20 mm × 1.5 mm mold and sealed in a humidity chamber

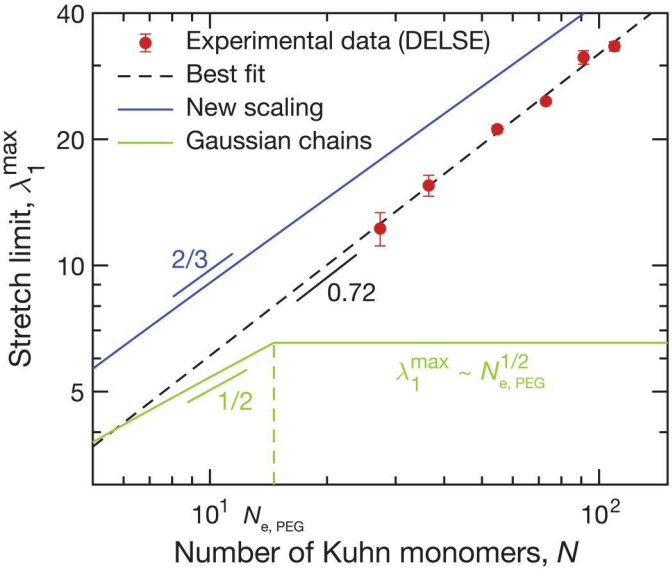

Fig. 4. Increased stretchability of the DELSE. The stretchability of the DELSE at 60°C scales indefinitely with $N^{0.72}$, exceeding the limits of common elastomers, which scale with $N^{1/2}$ and saturate at $N_e^{1/2}$ due to trapped entanglements. Error bars denote standard deviations.

for 12 hours to support amide bond formation. Reaction efficiency was evaluated in the gel state by comparing the as-prepared shear modulus to phantom network theory by the procedure presented by Lin *et al.* (*32*) for tetra-PEG gels. The drying process began once the gels were fully synthesized. Samples were removed from the humidity chamber and placed on an acrylic plate that was lubricated with a thin layer of silicone oil to mitigate residual stresses from surface adhesion. The covered plate was placed in an incubator for at least 2 hours to dehydrate and deswell the samples to the semicrystalline state. Samples were removed from the acrylic plate and heated on a hot plate above T_m (~45°C) to alleviate any anisotropy caused by environmental stresses during deswelling and then equilibrated to the proper measurement temperature. For one-to-one comparisons with the DELE, a second DELSE was fabricated at ~2c^* using the same protocol except with doubled PEG macromer concentrations. DELSE samples with chain molecular weights of 3750, 7500, 12,250, and 15,000 g/mol were achieved by combining A- and B-type tetrafunctional macromers with different molecular weights since only commercially available macromers were used in this study. The quantity of each solution was adjusted to ensure that the number of macromers was consistent between solutions with different molecular weights (e.g., 75 mg of 10,000 g/mol PEG-NH_2 in 0.75 ml of phosphate buffer mixed with 150 mg of 20,000 g/mol PEG-NHS in 1.5 ml of phosphate–citric acid buffer). The remainder of the synthesis process remained the same. The entanglement molecular weight of PEG in the dry condition is 2000 g/mol (*44*). Overall, the number of Kuhn monomers was determined by dividing the total chain molecular weight by the molar mass of a single Kuhn monomer (M_0^{Kuhn} = 137 g/mol for PEG) (*44*) as follows

$$N = M_W^{chain}/M_0^{Kuhn} \quad (1)$$

where N is the number of Kuhn monomers and M_W^{chain} is the molecular weight of a single polymer chain.

Fabrication of DELEs from small-molecule crosslinkers

The DELE network was formed from an A-B type reaction of commercially available trifunctional and bi-NHS–terminated PEG macromers (2arm-PEG-NHS, Laysan Bio) with 10,000 g/mol macromer molecular weights (fig. S1C). Bi-amine–terminated PEG (400 mg) was mixed with a 1-ml phosphate aqueous buffer with a pH of 7.4 and ionic strength of 100 mM. Next, 1 ml of phosphate–citric acid aqueous buffer with a pH of 5.8 and ionic strength of 100 mM was added. The solution was sonicated and mixed until the polymer completely dissolved. Trifunctional amine (4 mg) was added to the solution. The crosslinking condition was set to 2c^* since crosslinking at c^* during testing resulted in insufficient gelation for further processing. The DELSE was prepared at c^* and 2c^* for direct structural (fig. S10) and mechanical (fig. S16) comparisons with the DELE. The solution was quickly degassed and poured over a 40 mm × 20 mm × 1.5 mm mold and sealed in a humidity chamber for 12 hours to support amide bond formation. The drying process began once the gel was fully synthesized. The sample was removed from the humidity chamber and placed on an acrylic plate that was lubricated with a thin layer of silicone oil to mitigate residual stresses from surface adhesion. The covered plate was placed in an incubator for at least 2 hours to dehydrate the samples to the semicrystalline state. Samples were removed from the acrylic plate and heated on a hot plate above T_m (~45°C) to alleviate any anisotropy caused by environmental stresses during deswelling and then equilibrated to the proper measurement temperature.

Mechanical testing

All mechanical tests were performed in a silicone oil bath at 60°C using a U-Stretch apparatus (Cellscale) unless otherwise noted. Depending on the sample, either a 4.4-N or 44-N load cell was used. Unless otherwise noted, for mechanical tests, sample dimensions were approximately 1.5 mm × 7 mm × 0.6 mm, and the loading rate was 0.5 s^{-1}. Room temperature (22°C) mechanical tests on NR and PEG specimens (figs. S22 and S24) were performed in uniaxial tension (13 mm × 4.8 mm × 1.5 mm at 100 mm min^{-1} for NR, 13 mm × 1.5 mm × 0.5 mm at 100 mm min^{-1} for PEG) on a mechanical testing machine (Z2.5, Zwick/Roell) with a 2.5-kN load cell. Force F and gauge displacement Δ were output by the testing machine during loading. Nominal stress was evaluated as $S = F/(Wt)$, where W is the undeformed sample width and t is the sample thickness. Stretch was evaluated as $\lambda = (H + \Delta)/H$, where H is the undeformed sample height. Samples were fixed under mechanical pressure between grooved jaw clamps. Images were taken during sample loading to ensure that there was no slipping during loading and to validate stretch measurements. The distances between marks drawn on the sample were measured using ImageJ at various stretches from photographs for validation. Fracture energy was measured using the pure shear test method (*45*). The elastic energy density function $w(\lambda)$ was first evaluated by measuring the nominal stress at a given stretch during a monotonic stretch to failure of an intact sample. The breaking stretch λ_1^{max} was recorded as the measured stretch when the intact sample ruptured. An artificial notch was introduced perpendicular to the loading direction in a second sample by a blade. The cut length was approximately W/

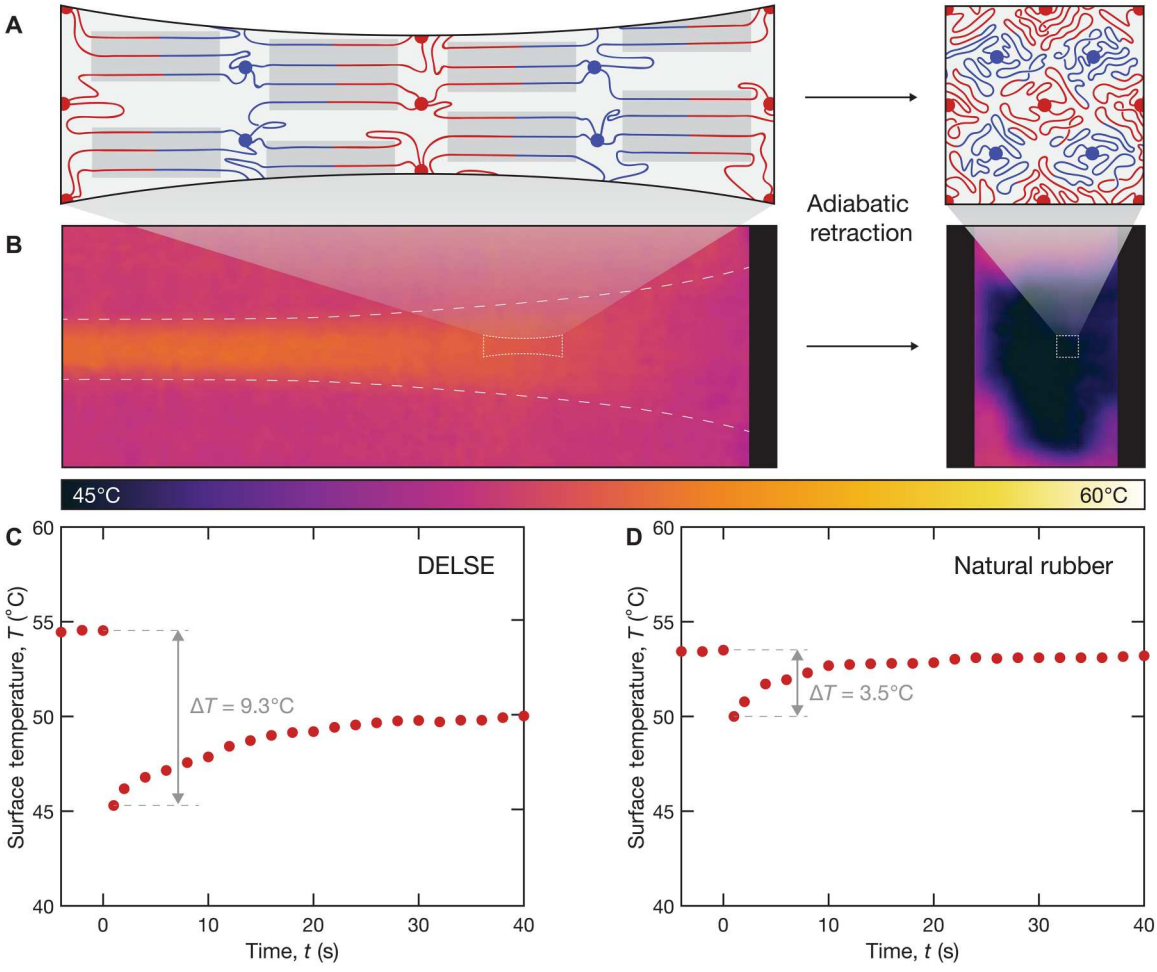

Fig. 5. Elastocaloric effect of the DELSE. (**A**) Schematics indicate the destruction of crystalline domains and disruption of polymer chain alignment during adiabatic retraction. (**B**) Thermal images of the DELSE during the retraction. The applied mechanical loading and measured surface temperature are recorded for the (**C**) DELSE and (**D**) NR during the retraction process.

3. The sample was monotonically loaded to failure, and the critical stretch λ_c was recorded as the stretch that induced crack propagation. The fracture energy was then evaluated as $\Gamma = w(\lambda_c)H$. Intact samples were cyclically loaded and unloaded to incrementally higher stretches to evaluate hysteretic effects.

DMA testing

DMA was performed on fiber specimens of the DELSE (crosslinked at ~c^* and ~$2c^*$) and DELE (crosslinked at ~$2c^*$) using a DMA Q800 testing device (TA Instruments) equilibrated to and tested at 60°C (see results in fig. S16). DELSE (~c^*) and DELE networks have similar storage moduli (E') across the frequency range of 0.1 to 10 Hz, suggesting that the elastically active strands between crosslinks are comparable between these two networks. The E' of the DELSE remains rate independent, while the E' of the DELE slightly increases with frequency, which indicates that the DELSE contains less defects than the DELE. The large difference (two orders of magnitude) between the storage (E') and loss (E'') moduli further reinforces that the DELSE has a low fraction of defects. The low loss moduli of DELSE samples are consistent with the low hysteresis observed in cyclic loading in figs. S14 and S15. Although they have similar E', the E'' of the DELSE is an order of magnitude smaller than that of the DELE. Relatively large E'' for the DELE is consistent with the large hysteresis observed in fig. S15C, further suggesting that the network contains more elastically inactive defects compared to the DELSE. Although the loss moduli of the DELE and DELSE are over an order of magnitude different, the frequency dependence of the loss moduli is very similar: the DELSE has a slope of 0.15, while the DELE has a slope of 0.14. According to the model developed by Curro and Pincus, similar frequency dependence indicates that the dangling polymer structures have similar size compared to the network mesh formed by elastically active strands between crosslinks in the DELSE and DELE (*46*, *47*).

X-ray scattering

SAXS and WAXS were performed using a large-area 2D Dectris Pilatus3R 300K detector centered on samples within a SAXSLAB apparatus (X-ray Diffraction Shared Experimental Facility at Massachusetts Institute of Technology). The vacuum chamber was pumped to 0.08 mbar during measurements to reduce background intensity fluctuation. Proper sample and beamstop alignment were tested before measurement. Details on measurement

configurations are listed in table S1. Tensile specimens (approximately 4 mm × 1 mm × 0.6 mm) were stretched for bulk structural characterization using the same procedure described for mechanical testing before x-ray measurement. DELSE specimens were cooled to room temperature and fixed on either end with Krazy glue to an acrylic mount. The custom mount was designed to fix samples in the deformed state while enabling direct contact between the sample surface and the heating apparatus. Samples were conductively heated by a Linkam heating stage (Scientific Instruments Ltd.) for steady-state heated measurements. All applied temperature changes using the heating stage occurred at a rate of 10°C/min. Temperature effects were mitigated by enabling sufficient time for samples to reach steady state. The effect of thermal history was evaluated to validate this procedure (see fig. S9). All samples were oriented such that the stretching direction was aligned vertically with the sample holder.

Notched specimens were stretched using the same procedure except were in the pure shear configuration to evaluate SIC near the crack tip. The position of the crack tip was chosen with uncertainty of ±50 μm from trial measurements near the edge position. The crack was positioned perpendicular to the stretching direction. The sample was shifted horizontally by 0.2 mm between measurements. Measurements were performed at 55°C once the sample reached its thermal steady state. The SAXS aperture sizes were selected for measurement in the WAXS regime to constrict the measurement spot to the area of interest since the crystallinity varies as a function of position.

The 2D SAXS and WAXS scans were converted to 1D intensity profiles for interpretation of crystallinity index by averaging over all azimuthal angles. Although some reported crystallinity measurements average over a small azimuthal range, we counter that this strategy causes inflated crystallinity measurements in anisotropic samples. Averaging over all angles was selected to reduce this error and was validated by the 2D convolution scheme developed to distinguish orientation in amorphous and crystalline domains. Direct comparisons in crystallinity measurements with published data follow the reported protocol for the given result. The average intensity measured during scattering was plotted against the scattering angle 2θ, which relates to the scattering vector q as follows

$$q = \frac{4\pi \sin(2\theta/2)}{\Lambda} \tag{2}$$

where Λ is the x-ray wavelength.

This quantity relates to the characteristic interplanar d-spacing through Bragg′s law, which is defined as

$$2d\ \sin\theta = n\Lambda \tag{3}$$

where d is the interplanar spacing and n is the diffraction order.

Diffraction spots were indexed according to their d-spacing and the associated crystal lattice configuration.

$$d_{hkl} = \frac{2\pi}{h\boldsymbol{a} + k\boldsymbol{b} + l\boldsymbol{c}} \tag{4}$$

where h, k, and l are Miller indices, and $\boldsymbol{a}$, $\boldsymbol{b}$, and $\boldsymbol{c}$ are the basis of vectors for the reciprocal lattice.

The crystallinity index was evaluated by fitting Gaussian or pseudo-Voigt curves to the amorphous and crystalline peaks distinguished from the 1D intensity profile after subtracting the background scattering intensity. Summing the areas under the fitted curves enables deduction of the crystallinity index as follows

$$\chi = \frac{A_C}{A_C + A_A} \tag{5}$$

where A_C is the area under the crystalline peaks and A_A is the area under amorphous peaks.

The isotropic and anisotropic contributions were deconvolved from the 2D WAXS patterns following a similar treatment to reported protocols (*18*, *37*, *38*). The background scattering intensity was first subtracted. The 2D Cartesian WAXS pattern was then converted into a 2D polar WAXS plot. At each azimuthal angle ϕ, a peak fitting routine was performed to the amorphous and crystalline diffraction peaks using either a Gaussian or pseudo-Voigt function. The fit curves were stored at each angle. The total crystalline and amorphous peak contributions were evaluated by discretely summing the areas of fitted peaks across all angles throughout the 2D polar WAXS pattern, giving effective crystalline and amorphous peak volumes. The crystallinity index was then calculated classically by replacing the 1D amorphous and crystalline peak areas in eq. S4 with 2D peak volumes.

The isotropic contribution of the amorphous and crystalline phases was first determined as the minimum contribution present at all angles. The anisotropic contribution of both phases at a given azimuthal angle was determined using the following equation

$$A_{an}(q, \phi) = A_{tot} - A_{iso}(q) \tag{6}$$

where A_{an} is the anisotropic scattering contribution, A_{tot} is the total scattering intensity, and A_{iso} is the isotropic scattering contribution. With a known crystallinity index, the isotropic and anisotropic fractions of each phase were determined by summing the areas across all azimuthal angles and comparing these volumes. The deconvolution scheme is detailed in fig. S8.

The orientation of the crystalline regime was determined from the azimuthal spread of intensity at the d-spacing corresponding to a given diffraction peak (*48*). Orientation was defined for a peak at given Miller indices from a 2D WAXS pattern as follows

$$\langle \cos^2\phi \rangle_{hkl} = \frac{\int_0^{\pi/2} I(\phi)\cos^2\phi \sin\phi d\phi}{\int_0^{\pi/2} I(\phi)\sin\phi d\phi} \tag{7}$$

where $I(\phi)$ is the intensity as a function of the azimuthal angle ϕ.

The Hermans′ orientation parameter f_2 was determined from this orientation measure as follows

$$f_2 = \frac{3\langle \cos^2\phi \rangle - 1}{2} \tag{8}$$

where f_2 takes the value −0.5 when the crystal is aligned perpendicular to the direction of interest, 0 when there is no preferred direction, and 1 when aligned parallel to the reference direction.

The apparent crystallite size was determined through the 1D peak fitting scheme using the Scherrer equation.

$$D = \frac{K\Lambda}{B(2\theta)\cos\theta} \tag{9}$$

where D is the apparent crystallite size, K is the Scherrer constant or

shape factor [K= 0.94 for full width at half maximum (FWHM) measurements], Λ is the x-ray wavelength, B is the breadth or FWHM of the 1D profile fit to the peak at a given value of 2θ, and θ is the Bragg angle for the selected peak. The DELSE and DELE both displayed peak apparent crystallite sizes of about 22 nm, as measured from the (120) diffraction spot.

DSC measurement

DSC was performed on the DELSE to assess the melting temperature T_m and heat flow characteristics. A differential scanning calorimeter (DSC 2500, TA Instruments) with a refrigerated cooling system (RSC90, TA Instruments) measured heat flow as a function of time and temperature. Between 5 and 10 mg of the DELSE sample was placed in a Tzero Pan during the measurements. Heating and cooling cycles occurred from 30° to 90°C at a rate of 10°C min^{-1}. The melting temperature was extrapolated from the endothermic peak during heating, as shown in fig. S21.

Elastocaloric cooling measurement

The elastocaloric effect was induced by rapid stretching and retraction of the DELSE and NR specimens in a gravity convection oven (EQ-DFA-7000, MTI Corporation) above 50°C. A custom remote-control stretching device was constructed to rapidly stretch and retract specimens. Grooved jaw clamps were mounted to a linear actuator to extend at a constant speed of 50 mm/s with a 20 N maximum load. Sample dimensions were selected such that the stretching rate reached about 15 s^{-1} for stretching and retraction, so adiabaticity was assumed for both processes (*15*). The linear actuator enabled application of a uniaxial applied stress to the sample when mounted on opposing ends with the metal jaw clamps. The stretch was calculated from the measured initial and known deformed length. The stretching device was connected to a controller and power supply. The entire assembly was placed in the oven during measurement, and a wireless remote was activated to stretch and retract samples from outside of the heated chamber. A FLIR C5 thermal imager (FLIR Systems) was placed in the convection oven to record and output the sample surface temperature during mechanical stretching. The emissivity was set at a constant of 0.95 for all measurements. Samples were mounted and placed in the enclosed oven for at least 20 min to achieve steady state before measurement. It is noteworthy that measurement error may have occurred due to the precision of the thermal imager, uncertainty in linear actuation speed, battery performance at elevated temperatures, and temperature consistency throughout the oven.

Supplementary Materials

This PDF file includes:

Supplementary Text
Figs. S1 to S24
Tables S1 to S4
References

REFERENCES AND NOTES

1. J. R. Katz, X-ray spectrography of polymers and in particular those having a rubber-like extensibility. *Trans. Faraday Soc.* **32**, 77–94 (1936).
2. H. P. Zhang, J. Niemczura, G. Dennis, K. Ravi-Chandar, M. Marder, Toughening effect of strain-induced crystallites in natural rubber. *Phys. Rev. Lett.* **102**, 245503 (2009).
3. M. Tosaka, S. Murakami, S. Poompradub, S. Kohjiya, Y. Ikeda, S. Toki, I. Sics, B. S. Hsiao, Orientation and crystallization of natural rubber network as revealed by WAXD using synchrotron radiation. *Macromolecules* **37**, 3299–3309 (2004).
4. S. Toki, T. Fujimaki, M. Okuyama, Strain-induced crystallization of natural rubber as detected real-time by wide-angle X-ray diffraction technique. *Polymer* **41**, 5423–5429 (2000).
5. J. Y. Sun, X. Zhao, W. R. K. Illeperuma, O. Chaudhuri, K. H. Oh, D. J. Mooney, J. J. Vlassak, Z. Suo, Highly stretchable and tough hydrogels. *Nature* **489**, 133–136 (2012).
6. J. P. Gong, Y. Katsuyama, T. Kurokawa, Y. Osada, Double-network hydrogels with extremely high mechanical strength. *Adv. Mater.* **15**, 1155–1158 (2003).
7. E. Ducrot, Y. Chen, M. Bulters, R. P. Sijbesma, C. Creton, Toughening elastomers with sacrificial bonds and watching them break. *Science* **344**, 186–189 (2014).
8. Y. Yang, Z. Song, G. Lu, Q. Zhang, B. Zhang, B. Ni, C. Wang, X. Li, L. Gu, X. Xie, H. Gao, J. Lou, Intrinsic toughening and stable crack propagation in hexagonal boron nitride. *Nature* **594**, 57–61 (2021).
9. E. Filippidi, T. R. Cristiani, C. D. Eisenbach, J. Herbert Waite, J. N. Israelachvili, B. Kollbe Ahn, M. T. Valentine, Toughening elastomers using mussel-inspired iron-catechol complexes. *Science* **358**, 502–505 (2017).
10. N. Domun, H. Hadavinia, T. Zhang, T. Sainsbury, G. H. Liaghat, S. Vahid, Improving the fracture toughness and the strength of epoxy using nanomaterials—A review of the current status. *Nanoscale* **7**, 10294–10329 (2015).
11. J. Kim, G. Zhang, M. Shi, Z. Suo, Fracture, fatigue, and friction of polymers in which entanglements greatly outnumber cross-links. *Science* **374**, 212–216 (2021).
12. C. Liu, N. Morimoto, L. Jiang, S. Kawahara, T. Noritomi, H. Yokoyama, K. Mayumi, K. Ito, Tough hydrogels with rapid self-reinforcement. *Science* **372**, 1078–1081 (2021).
13. T. Fujiyabu, N. Sakumichi, T. Katashima, C. Liu, K. Mayumi, U. Il Chung, T. Sakai, Tri-branched gels: Rubbery materials with the lowest branching factor approach the ideal elastic limit. *Sci. Adv.* **8**, eabk0010 (2022).
14. F. Greibich, R. Schwödiauer, G. Mao, D. Wirthl, M. Drack, R. Baumgartner, A. Kogler, J. Stadlbauer, S. Bauer, N. Arnold, M. Kaltenbrunner, Elastocaloric heat pump with specific cooling power of 20.9 W g^{-1} exploiting snap-through instability and strain-induced crystallization. *Nat. Energy* **6**, 260–267 (2021).
15. S. Zhang, Q. Yang, C. Li, Y. Fu, H. Zhang, Z. Ye, X. Zhou, Q. Li, T. Wang, S. Wang, W. Zhang, C. Xiong, Q. Wang, Solid-state cooling by elastocaloric polymer with uniform chain-lengths. *Nat. Commun.* **13**, 9 (2022).
16. R. Wang, S. Fang, Y. Xiao, E. Gao, N. Jiang, Y. Li, L. Mou, Y. Shen, W. Zhao, S. Li, A. F. Fonseca, D. S. Galvão, M. Chen, W. He, K. Yu, H. Lu, X. Wang, D. Qian, A. E. Aliev, N. Li, C. S. Haines, Z. Liu, J. Mu, Z. Wang, S. Yin, M. D. Lima, B. An, X. Zhou, Z. Liu, R. H. Baughman, Torsional refrigeration by twisted, coiled, and supercoiled fibers. *Science* **366**, 216–221 (2019).
17. C. Lang, E. C. Lloyd, K. E. Matuszewski, Y. Xu, V. Ganesan, R. Huang, M. Kumar, R. J. Hickey, Nanostructured block copolymer muscles. *Nat. Nanotechnol.* **17**, 752–758 (2022).
18. S. Toki, B. S. Hsiao, Nature of strain-induced structures in natural and synthetic rubbers under stretching. *Macromolecules* **36**, 5915–5917 (2003).
19. S. Lin, J. Liu, X. Liu, X. Zhao, Muscle-like fatigue-resistant hydrogels by mechanical training. *Proc. Natl. Acad. Sci. U.S.A.* **116**, 10244–10249 (2019).
20. M. Hua, S. Wu, Y. Ma, Y. Zhao, Z. Chen, I. Frenkel, J. Strzalka, H. Zhou, X. Zhu, X. He, Strong tough hydrogels via the synergy of freeze-casting and salting out. *Nature* **590**, 594–599 (2021).
21. R. B. Dupaix, M. C. Boyce, Finite strain behavior of poly(ethylene terephthalate) (PET) and poly(ethylene terephthalate)-glycol (PETG). *Polymer* **46**, 4827–4838 (2005).
22. X. Liao, M. Dulle, J. M. De Souza, E. Silva, R. B. Wehrspohn, S. Agarwal, S. Förster, H. Hou, P. Smith, A. Greiner, High strength in combination with high toughness in robust and sustainable polymeric materials. *Science* **366**, 1376–1379 (2019).
23. G. J. Dunderdale, S. J. Davidson, A. J. Ryan, O. O. Mykhaylyk, Flow-induced crystallisation of polymers from aqueous solution. *Nat. Commun.* **11**, 3372 (2020).
24. J. Gough, VII. A description of a property of caoutchouc, or indian rubber; with some reflections on the cause of the elasticity of this substance. In a letter to Dr. Holme. *Philos. Mag.* **24**, 39–43 (1805).
25. T. Sakai, T. Matsunaga, Y. Yamamoto, C. Ito, R. Yoshida, S. Suzuki, N. Sasaki, M. Shibayama, U.-i. Chung, Design and fabrication of a high-strength hydrogel with ideally homogeneous network structure from tetrahedron-like macromonomers. *Macromolecules* **41**, 5379–5384 (2008).
26. Y. Nomoto, T. Matsunaga, T. Sakai, M. Tosaka, M. Shibayama, Structure and physical properties of dried Tetra-PEG gel. *Polymer* **52**, 4123–4128 (2011).
27. T. Yamamoto, J. A. Campbell, S. Panyukov, M. Rubinstein, Scaling theory of swelling and deswelling of polymer networks. *Macromolecules* **55**, 3588–3601 (2022).
28. H. M. James, E. Guth, Theory of the increase in rigidity of rubber during cure. *J. Chem. Phys.* **15**, 669–683 (1947).
29. Y. Akagi, T. Katashima, H. Sakurai, U. Il Chung, T. Sakai, Ultimate elongation of polymer gels with controlled network structure. *RSC Adv.* **3**, 13251–13258 (2013).

30. M. C. Boyce, E. M. Arruda, Constitutive models of rubber elasticity: A review. *Rubber Chem. Technol.* **73**, 504–523 (2000).
31. L. R. G. Treloar, *The Physics of Rubber Elasticity* (Oxford Univ. Press, 1975).
32. S. Lin, J. Ni, D. Zheng, X. Zhao, Fracture and fatigue of ideal polymer networks. *Extreme Mech. Lett.* **48**, 101399 (2021).
33. K. Urayama, S. Kohjiya, Uniaxial elongation of deswollen polydimethylsiloxane networks with supercoiled structure. *Polymer* **38**, 955–962 (1997).
34. H. Tadokoro, Y. Chatani, T. Yoshihara, S. Tahara, S. Murahashi, Structural studies on polyethers, [-(CH2)m-O-]n. *II. Molecular structure of polyethylene oxide. Makromol. Chem.* **73**, 109–127 (1964).
35. Y. Takahashi, I. Sumita, H. Tadokoro, Structural studies of polyethers. IX. Planar zigzag modification of poly(ethylene oxide). *J. Polym. Sci. Polym. Phys. Ed.* **11**, 2113–2122 (1973).
36. Y. Takahashi, H. Tadokoro, Structural studies of polyethers, (–(CH2)m–O–)n. X. Crystal structure of poly(ethylene oxide). *Macromolecules* **6**, 672–675 (1973).
37. S. Ran, D. Fang, X. Zong, B. S. Hsiao, B. Chu, P. M. Cunniff, Structural changes during deformation of Kevlar fibers via on-line synchrotron SAXS/WAXD techniques. *Polymer* **42**, 1601–1612 (2001).
38. S. Toki, I. Sics, S. Ran, L. Liu, B. S. Hsiao, S. Murakami, K. Senoo, S. Kohjiya, New insights into structural development in natural rubber during uniaxial deformation by in situ synchrotron X-ray diffraction. *Macromolecules* **35**, 6578–6584 (2002).
39. G. Nian, J. Kim, X. Bao, Z. Suo, Making highly elastic and tough hydrogels from doughs. *Adv. Mater.* **34**, e2206577 (2022).
40. T. Katashima, M. Asai, K. Urayama, U. Il Chung, T. Sakai, Mechanical properties of tetra-PEG gels with supercoiled network structure. *J. Chem. Phys.* **140**, 074902 (2014).
41. Z. Xie, G. Sebald, D. Guyomar, Temperature dependence of the elastocaloric effect in natural rubber. *Phys. Lett. A* **381**, 2112–2116 (2017).
42. Y. Akagi, H. Sakurai, J. P. Gong, U. Il Chung, T. Sakai, Fracture energy of polymer gels with controlled network structures. *J. Chem. Phys.* **139**, 144905 (2013).
43. T. Matsunaga, T. Sakai, Y. Akagi, U. Il Chung, M. Shibayama, Structure characterization of tetra-PEG gel by small-angle neutron scattering. *Macromolecules* **42**, 1344–1351 (2009).
44. M. Rubinstein, R. H. Colby, *Polymer Physics* (Oxford Univ. Press, 2003).
45. R. S. Rivlin, A. G. Thomas, Rupture of rubber. I. Characteristic energy for tearing. *J. Polym. Sci.* **10**, 291–318 (1953).
46. P. J. Flory, M. Volkenstein, *Statistical Mechanics of Chain Molecules* (Interscience Publishers, 1969), pp. 699–700.
47. L. H. Cai, T. E. Kodger, R. E. Guerra, A. F. Pegoraro, M. Rubinstein, D. A. Weitz, Soft poly (dimethylsiloxane) elastomers from architecture-driven entanglement free design. *Adv. Mater.* **27**, 5132–5140 (2015).
48. Z. W. Wilchinsky, Measurement of orientation in polypropylene film. *J. Appl. Phys.* **31**, 1969–1972 (1960).
49. T. E. Gartner, A. Jayaraman, Modeling and simulations of polymers: A roadmap. *Macromolecules* **52**, 755–786 (2019).
50. C. W. Barney, Z. Ye, I. Sacligil, K. R. McLeod, H. Zhang, G. N. Tew, R. A. Riggleman, A. J. Crosby, Fracture of model end-linked networks. *Proc. Natl. Acad. Sci. U.S.A.* **119**, e2112389119 (2022).
51. E. Wang, F. A. Escobedo, Mechanical properties of tetrapolyethylene and tetrapoly(ethylene oxide) diamond networks via molecular dynamics simulations. *Macromolecules* **49**, 2375–2386 (2016).
52. E. Wang, F. Escobedo, Swelling and tensile properties of tetra-polyethylene glycol via coarse-grained molecular models. *Macromol. Theory Simul.* **26**, 1600098 (2017).
53. Y. Higuchi, Fracture processes of crystalline polymers using coarse-grained molecular dynamics simulations. *Polym. J.* **50**, 579–588 (2018).
54. Y. Yin, N. Bertin, Y. Wang, Z. Bao, W. Cai, Topological origin of strain induced damage of multi-network elastomers by bond breaking. *Extreme Mech. Lett.* **40**, 100883 (2020).
55. K. Kremer, G. S. Grest, Dynamics of entangled linear polymer melts: A molecular-dynamics simulation. *J. Chem. Phys.* **92**, 5057–5086 (1990).
56. J. D. Weeks, D. Chandler, H. C. Andersen, Role of repulsive forces in determining the equilibrium structure of simple liquids. *J. Chem. Phys.* **54**, 5237–5247 (1971).
57. R. Faller, A. Kolb, F. Müller-Plathe, Local chain ordering in amorphous polymer melts: Influence of chain stiffness. *Phys. Chem. Chem. Phys.* **1**, 2071–2076 (1999).
58. R. Faller, F. Müller-Plathe, A. Heuer, Local reorientation dynamics of semiflexible polymers in the melt. *Macromolecules* **33**, 6602–6610 (2000).
59. R. Faller, F. Müller-Plathe, Chain stiffness intensifies the reptation characteristics of polymer dynamics in the melt. *ChemPhysChem* **2**, 180–184 (2001).
60. R. Everaers, H. A. Karimi-Varzaneh, F. Fleck, N. Hojdis, C. Svaneborg, Kremer-grest models for commodity polymer melts: Linking theory, experiment, and simulation at the kuhn scale. *Macromolecules* **53**, 1901–1916 (2020).
61. A. P. Thompson, H. M. Aktulga, R. Berger, D. S. Bolintineanu, W. M. Brown, P. S. Crozier, P. J. t'Veld, A. Kohlmeyer, S. G. Moore, T. D. Nguyen, R. Shan, M. J. Stevens, J. Tranchida, C. Trott, S. J. Plimpton, LAMMPS - a flexible simulation tool for particle-based materials modeling at the atomic, meso, and continuum scales. *Comput. Phys. Commun.* **271**, 108171 (2022).
62. A. I. Jewett, D. Stelter, J. Lambert, S. M. Saladi, O. M. Roscioni, M. Ricci, L. Autin, M. Maritan, S. M. Bashusqeh, T. Keyes, R. T. Dame, J. E. Shea, G. J. Jensen, D. S. Goodsell, Moltemplate: A tool for coarse-grained modeling of complex biological matter and soft condensed matter physics. *J. Mol. Biol.* **433**, 166841 (2021).
63. L. Martínez, R. Andrade, E. G. Birgin, J. M. Martínez, PACKMOL: A package for building initial configurations for molecular dynamics simulations. *J. Comput. Chem.* **30**, 2157–2164 (2009).
64. J. R. Gissinger, B. D. Jensen, K. E. Wise, Modeling chemical reactions in classical molecular dynamics simulations. *Polymer* **128**, 211–217 (2017).
65. J. R. Gissinger, B. D. Jensen, K. E. Wise, Reacter: A heuristic method for reactive molecular dynamics. *Macromolecules* **53**, 9953–9961 (2020).
66. R. Auhl, R. Everaers, G. S. Grest, K. Kremer, S. J. Plimpton, Equilibration of long chain polymer melts in computer simulations. *J. Chem. Phys.* **119**, 12718–12728 (2003).
67. E. M. Arruda, M. C. Boyce, A three-dimensional constitutive model for the large stretch behavior of rubber elastic materials. *J. Mech. Phys. Solids* **41**, 389–412 (1993).

Acknowledgments: We thank J. Cox and C. Settens for help with x-ray diffraction and B. Li for feedback on elastocaloric cooling experiments. We acknowledge the MIT SuperCloud and Lincoln Laboratory Supercomputing Center for providing high-performance computing resources. **Funding:** This work was supported in part by the National Institutes of Health (1R01HL153857-01, 1R01HL167947-01, and P01-HL164320), the National Science Foundation (EFMA-1935291), and the Department of Defense Congressionally Directed Medical Research Programs (PR200524P1). C.M.H. acknowledges financial support from the NSF Graduate Research Fellowship, the Warren M. Rohsenow Fellowship, and the Epp and Ain Sonin Fellowship. J.H.Z. acknowledges financial support from the Adbul Latif Jameel Water and Food Systems Lab (JWAFS) Graduate Fellowship. **Author contributions:** Conceptualization: X.Z., S.L., and C.M.H. Methodology: X.Z., C.M.H., S.L., J.H.Z., and S.W. Investigation: C.M.H. and J.H.Z. Visualization: C.M.H., X.Z., S.L., J.H.Z., and S.W. Software: J.H.Z. and C.M.H. Formal analysis: C.M.H. and J.H.Z. Funding acquisition: X.Z. Project administration: X.Z. and M.R. Supervision: X.Z. and M. R. Writing—original draft: C.M.H., S.L., X.Z., and J.H.Z. Writing—review and editing: C.M.H., S.L., X.Z., J.H.Z., S.W., and M.R. **Competing interests:** The authors declare that they have no competing interests. **Data and materials availability:** All data needed to evaluate the conclusions in the paper are present in the paper and/or the Supplementary Materials.

Submitted 2 June 2023
Accepted 15 November 2023
Published 13 December 2023
10.1126/sciadv.adj0411